Korean Journal of Chemical Engineering (2024) 41:1375–1389
https://doi.org/10.1007/s11814-024-00022-7

ORIGINAL ARTICLE

Modified Cu–ZnO Catalysts Supported on the Mixture of ZnO and Zn–Al Oxide for Methanol Production via Hydrogenation of CO and CO_2 Gas Mixture

Hyun-tae Song[1,2] · Hyun Dong Kim[1,3] · Yu-jeong Yang[1,3] · Jeong Min Seo[1,3] · Ye-na Choi[1,3] · Kwan-Young Lee[3] · Dong Ju Moon[1,2,3]

Received: 17 October 2023 / Revised: 30 November 2023 / Accepted: 2 December 2023 / Published online: 1 March 2024

Abstract

Cu-based catalysts were created using a two-step co-precipitation method, which can produce methanol from synthesis gases (H_2 and CO) that also contain CO_2. The catalysts were manufactured by a two-step co-precipitation method and compared with catalysts manufactured by a one-step co-precipitation method. The supports with Zn/Al = 1 (10ZA) and Zn/Al = 2 (20ZA) showed higher $ZnAl_2O_4$ ratios than the other catalysts, and the catalysts using these supports showed a similar trend to the $ZnAl_2O_4$ ratio. Cu–ZnO/mixture ZnO and $ZnAl_2O_4$ catalysts with more $ZnAl_2O_4$ (C10Z/20ZA and C20Z/10ZA) showed lower carbon and CO conversion losses and lower sintering of Cu (200) particles at the reaction temperatures (250, 300, and 350 °C) than the Cu–ZnO-$ZnAl_2O_4$ (C30ZA) catalyst. Cu–ZnO/mixture ZnO and $ZnAl_2O_4$ using support with Zn/Al = 2 (C10Z/20ZA) achieved dispersion of Cu (44.2%) and a methanol yield (409.0 $g_{MeOH}/kg_{cat.}/h$) at a reaction temperature of 250 °C, GHSV of 4,444 h^{-1}, and 40 bar.

Keywords Methanol synthesis · Copper catalyst · Zinc-alumina oxide spinel · CO/CO_2 gas mixture · Thermal stability of catalyst

List of Symbols

Av	Avogadro's number
D	Dispersion
D^*	True dispersion
DI	Deionized water
FID	Flame ionization detector
MW_{Cu}	Atomic weight of copper
N_{Cu}	Number of surface copper atoms in the unit surface area
S_{Cu}	Copper metal surface area per unit weight of the catalyst
S_p	Carbon selectivity
TCD	Thermal conductivity detector
$wt_{Cu}\%$	Copper content of the catalyst
X_i	Carbon conversion

Hyun-tae Song and Hyun Dong Kim have contributed equally to this study.

✉ Dong Ju Moon
djmoon@kist.re.kr

Hyun-tae Song
shtcwzz@gmail.com

Hyun Dong Kim
hyundongplus@gmail.com

Yu-jeong Yang
yyj5325@gmail.com

Jeong Min Seo
realitybestever21@gmail.com

Ye-na Choi
cyn990327@kist.re.kr

Kwan-Young Lee
kylee@korea.ac.kr

[1] Clean Energy Research Center, Korea Institute of Science and Technology (KIST), Hwarang-Ro 14-Gil 5, Seongbuk-Gu, Seoul 02792, Republic of Korea

[2] Division of Energy and Environment Technology, KIST School, Korea University of Science and Technology (UST), Hwarang-Ro 14-Gil 5, Seongbuk-Gu, Seoul 02792, Republic of Korea

[3] Department of Chemical & Biological Engineering, Korea University, 145 Anam-ro, Seongbuk-gu, Seoul, 02841, Republic of Korea

Introduction

Methanol is an important chemical that is used to produce formaldehyde, dimethyl ether (DME), and acetic acid. It is derived from crude oil and used for various daily purposes or as a major industrial material. Moreover, most hydrocarbons can be produced from methanol, making it a promising raw material for producing hydrocarbons that can replace crude oil [1]. Therefore, the development of catalysts and processes for methanol synthesis is crucial in the petrochemical industry. To address this growing demand, methanol production has been increased. Syngas used in methanol production is derived from natural gas through a catalytic reforming reaction, which is a widely used industrial process. The main reaction in methanol synthesis, which includes the hydrogenation of CO and CO_2, is outlined by Eqs. 1 and 3 [2].

$$\text{Hydrogenation of } CO_2{:}\ CO_2 + 3H_2 \rightarrow CH_3OH + H_2O \ (\Delta H_{298K} = -49.5\ \text{kJ/mol}) \quad (1)$$

$$\text{Reverse Water Gas Shift}{:}\ CO_2 + H_2 \leftrightarrow CO + H_2O \ (\Delta H_{298K} = 41.2\ \text{kJ/mol}) \quad (2)$$

$$\text{Hydrogenation of CO}{:}(3) = (1) - (2){:}\ CO + 2H_2 \rightarrow CH_3OH \ (\Delta H_{298K} = -90.7\ \text{kJ/mol}) \quad (3)$$

The performance of the catalysts can be influenced by various metals and preparation methods. Consequently, research efforts have focused on creating efficient and innovative commercial catalysts for methanol synthesis [3]. The use of Cu-based catalysts is most prevalent for industrial methanol synthesis processes that involve hydrogenation of CO and CO_2 [4, 5]. In 1920, ASF developed a Cr_2O_3/ZnO catalyst for methanol synthesis using CO and H_2. Subsequently, the ICI Company (Johnson Matty) invented a commercial Cu/ZnO/Al_2O_3 catalyst for methanol synthesis [6]. As the Cu specific surface area increases on Cu-based catalysts, the CO and CO_2 conversions and MeOH productivity of the catalysts increase in the MeOH synthesis reaction [7, 8]. Although methanol synthesis has been studied in many instances, there are thermodynamic limitations to this process [9]. The purpose of the ZnO support is to enhance copper dispersion and stabilize the active sites by preventing copper particle aggregation [10, 11]. To develop an effective Cu–Zn-based catalyst, it is important to ensure long-term stability by reducing deactivation factors such as sintering [8]. Although there has been limited research on the use of aluminum as a promoter, it is widely recognized that aluminum is an effective promoter for copper-based catalysts. It can stabilize the dispersed Cu/ZnO structure and slow the sintering of copper particles [12]. To develop Cu–Zn based catalysts for methanol synthesis, it is important to understand the effects of various metals and their preparation methods [3, 13]. Ren et al. prepared CuO/ZnO/Al_2O_3 using a co-precipitation method, and the precursor concentration was found to affect the structural characteristics of the catalyst. The dispersion of the precipitate increased as the precursor concentration decreased because of an improvement in the porosity of the catalyst [14]. Nilsson et al. used CO and CO_2 hydrogenation conditions to study the activation and surface reactions of CO and H_2 in a spinel $ZnAl_2O_4$ catalyst. It was confirmed that CO and H_2 activation occurred at the aluminum and zinc sites of the $ZnAl_2O_4$ catalyst to produce methanol and DME, with reversible adsorption of hydrogen species [15]. Jiang et al. manufactured Zn–Al oxides with various Zn/Al ratios to study the direct methanol synthesis from CO_2 and confirmed that the formation of amorphous ZnO around the shell of the $ZnAl_2O_4$ spinel promoted the formation of H_2 toward faster methanol formation. As described above, there have been studies on methanol synthesis using a $ZnAl_2O_4$ catalyst composed of zinc and aluminum, but research on the effect of the $ZnAl_2O_4$ spinel structure on methanol synthesis using a Cu/Zn/Al catalyst is insufficient [16]. In our previous research, we analyzed a Cu–ZnO/Mixture of ZnO and Zn-Al oxide catalyst using a two-step co-precipitation method. During the methanol synthesis reaction, it was found that the presence of Zn-Al oxide spinel in the catalyst decreased Cu sintering at high temperatures (over 300 °C). These results suggest a direction for improving the durability and productivity of Cu-/ZnO-$ZnAl_2O_4$ catalysts by enhancing the thermal durability of the Cu particles and reducing the sintering properties [17]. Few studies have been conducted on the effect of $ZnAl_2O_4$ in Cu-based catalysts for methanol synthesis reactions. However, most of the studies experimented with a mixture of ZnO and $ZnAl_2O_4$ or impregnation with a small amount of Cu (under 20 wt%) on a commercial support containing $ZnAl_2O_4$ [17–21]. Therefore, it is difficult to compare the research results of Cu/ZnO and Zn-Al oxide catalysts with compositions similar to those of commercial Cu-based catalysts [18–20, 22]. Because the co-precipitation method has various variables depending on the manufacturing results, the Zn/Al ratio was used as the variable in this experiment. The existing catalyst manufacturing method for $ZnAl_2O_4$-based Cu-based catalysts is similar to the manufacturing method of Cu/mixture of ZnO and $ZnAl_2O_4$ (C/30ZA when manufactured by a two-step co-precipitation method) [17–21]. This technology can be applied to the manufacture of catalysts for MeOH synthesis reactions for methanol floating production, storage, and off-loading (MeOH-FPSO) systems that produce methanol in offshore gas fields, including CO_2 [23].

Table 1 Preparation of Mixture of ZnO and Zn-Al oxide supports and Cu–ZnO/mixture of ZnO and Zn–Al oxide catalysts using support with different the Zn/Al composition of supports

Catalyst code	Total molar Ratio of reagent [Cu: Zn: Al][a]	1st Step co-precipitation (Molar ratio)				2nd Co-precipitation (Molar ratio)				
		Cu	Zn	Al	Calcination Temp. [℃]	Cu	Zn	Support		Calcination Temp. [℃]
								Zn	Al	
C20Z/10ZA	55 : 30 : 10 [57.9 : 31.6 : 10.5]	–	10	10	500	55	20	10	10	280
C10Z/20ZA		–	20	10	500	55	10	10	10	280
C/30ZA		–	30	10	500	55	–	30	10	280
C30ZA		55	30	10	280	–	–	–		–

[a]Molar ratio of metal calculated using the reagent used for preparing the catalysts. Calcined on the air condition

Table 2 Metal molar ratios of the catalysts in different catalysts were determined by XRF and XPS analysis, and the crystallite size (Scherrer Eq.) for the reduced catalysts based on the XRD results

Sample name	Metal molar ratio (used reagents)[a]	Bulk component molar ratio (except C, O) XRF analysis result (mol %)[b]					Surface molar ratio (mol %)[c]		Copper weight fraction (%)[d] ($g_{Cu}/g_{Cat.}$)
	Cu: Zn: Al	Cu	Zn	Al	Cu/Zn	Zn/Al	Cu/Zn		
							Calcined	Reduced	
10ZA	0: 10: 10 [0: 50: 50]	–	49.1	50.9	–	1.0	–	–	
20ZA	0: 20: 10 [0: 66.7: 33.3]	–	68.1	31.9	–	2.1	–	–	
30ZA	0: 30: 10 [0: 75: 25]	–	68.9	31.1	–	2.2	–	–	
C20Z/10ZA	55: 30: 10 [57.9: 31.6: 10.5]	58.7	27.5	13.8	2.1	2.0	1.9	1.0	62.7
C10Z/20ZA		66.3	29.5	4.2	2.2	6.9	2.7	1.3	65.6
C/30ZA		56.1	27.0	16.9	2.1	1.6	2.3	0.7	61.6
C30ZA		57.8	30.3	11.9	1.9	2.5	1.5	1.0	61.4

[a]Molar ratio of metal calculated using the reagent used for preparing the catalysts

[b]Molar ratio (except C, O) of the bulk component was measured using XRF(F2) ZSX Primus II, KIST

[c]The surface of the calcined catalysts was measured using Nexsa XPS system (Thermo Scientific), KIST

[d]Weight fraction (%) of copper except C, O measured by XRF(F2) ZSX Primus II, KIST

Experimental

Preparation of Supports and Catalysts

$Cu(NO_3)_2{\cdot}3H_2O$ and $Zn(NO_3)_2{\cdot}6H_2O$ were supplied by JUNSEI Chemical (Tokyo, Japan), whereas $Al(NO_3)_3{\cdot}9H_2O$, $NaHCO_3$, and $Na_2(CO_3)_2$ were purchased from SAMCHUN Chemical (Seoul, Korea). The metal-based molar ratios of the reagents used in the support and catalyst manufacturing processes are summarized in Tables 1 and 2. The catalyst manufacturing method used in this study was the same as that reported previously [8, 17, 24].

The methods used to manufacture the supports and catalysts are summarized in Fig. 1 and Table 2. Mixture of ZnO and Zn–Al oxides supports was prepared using a co-precipitation method. Mixture of ZnO and Zn–Al oxide supports was manufactured using $Zn(NO_3)_2{\cdot}6H_2O$ and $Al(NO_3)_3{\cdot}9H_2O$. Three Zn/Al molar ratios (1, 2, and 3) were dissolved in deionized (DI) water to obtain 1 M aqueous solutions. 1 M buffer solution was prepared by mixing $NaHCO_3$, Na_2CO_3, and DI water. Metal and base buffer solutions were added dropwise to DI water under intense stirring at 65 °C, and the pH was maintained at 6.5 ± 0.3. After the co-precipitation, the mixture was aged for 5 h with vigorous stirring at 65 °C. The mixture was then filtered and dried at 110 °C for 12 h. The dried precipitate was then calcined at 500 °C for 5 h in air. The three calcined supports at 500 °C were named 10ZA (Zn/Al = 1), 20ZA (Zn/Al = 2), and 30ZA (Zn/Al = 3), respectively.

Cu–Zn/Mixture of ZnO and Zn–Al oxide catalysts were prepared by secondary co-precipitation with mixture of ZnO and $ZnAl_2O_4$ supports (Fig. 1, Table 1). Before starting the catalyst manufacturing process, mixture of ZnO and Zn–Al oxide supports (10ZA, 20ZA, and 30ZA) was prepared and mixed with deionized (DI) water. $Cu(NO_3)_2{\cdot}3H_2O$ and $Zn(NO_3)_3{\cdot}6H_2O$ were mixed at a molar ratio of 55:X (X = 20, 10, 0). The mixture was dissolved in deionized (DI) water to obtain a 1 M aqueous solution. The amount of reagent was calculated, and a manufacturing experiment was performed

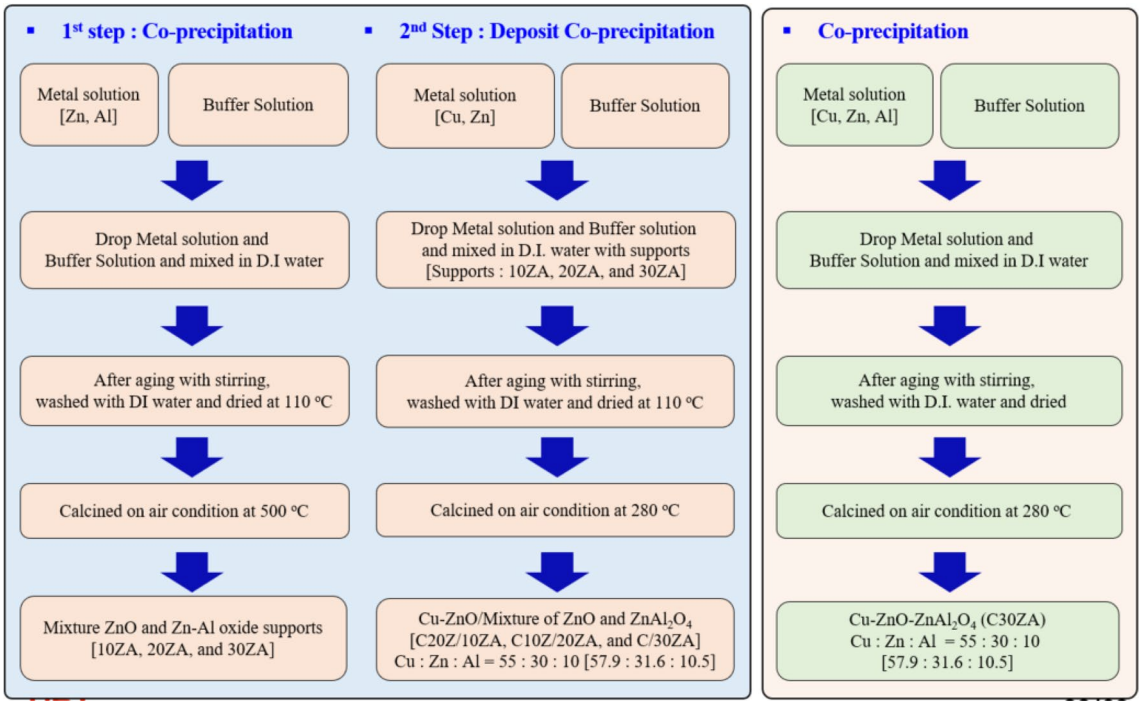

Fig. 1 Preparation of Cu–ZnO/mixture of ZnO and Zn-Al oxide catalyst which is manufactured using the Zn-Al oxide support that was produced by adjusting the Zn/Al composition of supports

such that the expected molar ratio of the elements in the Cu–Zn/mixture of ZnO and Zn–Al oxide prepared by the two-step co-precipitation method was Cu:Zn:Al = 55:30:10 [57.9:31.6:10.5 (mol%)]. 1 M base solution was composed of DI water mixed with $NaHCO_3$ and Na_2CO_3. The metal and base buffer solutions were then added dropwise to DI water under intense stirring at 65 °C, and the pH was maintained at 6.5 ± 0.3. After the co-precipitation, the mixture was aged for 5 h under vigorous stirring at 65 °C, filtered, and dried at 110 °C for 12 h. The dried precipitate was then calcined at 280 °C for 5 h in air. Prepared Cu–Zn/mixture of ZnO and Zn–Al oxide is denoted as C20Z/10ZA, C10Z/20ZA, and C/30ZA.

For comparison with Cu–Zn/Mixture of ZnO and Zn–Al oxide catalysts, a Cu–ZnO-$ZnAl_2O_4$ catalyst was prepared using a one-step co-precipitation method [8, 17, 24]. $Cu(NO_3)_2{\cdot}3H_2O$, $Zn(NO_3)_3{\cdot}6H_2O$, and $Al(NO_3)_3{\cdot}9H_2O$ were mixed at a molar ratio of 55:30:10 [57.9:31.6:10.5 (mol %)] and dissolved in DI water to form a 1 M solution. A 1 M buffer solution was prepared from DI water with $NaHCO_3$ and Na_2CO_3. The metal and buffer solutions were added dropwise to DI water under intense stirring at 65 °C, where the pH was maintained at 6.5 ± 0.3. After the co-precipitation, the solution was aged for 5 h with vigorous stirring at 65 °C, filtered, and dried at 110 °C for 12 h. The dried precipitate was calcined at 280 °C for 5 h under airflow. The calcined catalyst is denoted as C30ZA.

Sample Characterization

X-ray fluorescence (XRF) analysis was performed using the F2 ZSX Primus II at KIST. Component (Copper, Zinc, and Aluminum) molar and weight ratios were derived from the XRF analysis.

X-ray diffraction (XRD) analysis was performed using a D8 ADVANCE (LynxEye) XRD instrument (Netherlands) at KIST. It was operated at 40 kV and 40 mA using graphite-filtered Cu Kα radiation at a wavelength of 1.5406 nm with steps of 0.04° in the 2θ range of 10–90°. JADE software was used for XRD peak analysis. The Debye–Scherrer equation was used to calculate the size of the Cu particles. The reduced catalysts were prepared using a reactor system for N_2 physisorption and XRD analysis; they were produced in a 10% H_2/N_2 atmosphere at 270 °C (5 °C/min) for 2 h.

Brunauer–Emmett–Teller (BET) analysis was performed by N_2 physical adsorption and desorption analyses with Moonsorp-I (KIST, Korea) at the temperature of liquid N_2. The prepared supports, calcined catalysts, and reduced catalysts (0.1 g) were inserted into the instrument. Before the analysis, degassing was performed at 120 °C for 2 h to remove moisture. The surface areas of the samples were calculated using the BET analysis method. The total pore volume was calculated using the N_2 sorption and desorption capacities at $0.01 < P/P_0 < 0.99$. The average pore diameter

was calculated using the Brunauer–Emmett–Teller (BJH) method.

Temperature-Programmed Reduction (TPR) and N_2O titration were used to measure the H_2 reducibility of the calcined catalysts and N_2O oxidation of the reduced catalysts, and the surface areas of the Cu and Cu dispersions on the catalysts were calculated using two-step H_2-TPR results [25]. AutoChem II (Micromatics Inc., USA) was used for analysis. The catalyst samples (50 mg) were charged into the instrument using a U-type cell. In the pretreatment step, helium gas was passed through the samples at 120 °C for 2 h. The samples were cooled to 50 °C and maintained at that temperature for 1 h under 5% H_2 (Ar balance). In the first H_2-TPR, the sample was heated from 50 to 300 °C at a rate of 10 °C/min and 5% H_2 (Ar balance) at a flow rate of 50 ml/min. The outlet gas was passed through a TCD to obtain the TPR data. In the first H_2-TPR step, the CuO particles in the sample are converted to the Cu phase after H_2/Ar gas reduction. After the first H_2-TPR, the sample was cooled to 60 °C, while maintaining a He gas flow of 50 ml/min for 1 h. After cleaning, N_2O (50 ml/min) was flowed for N_2O chemisorption at 65 °C for 1 h. It is assumed that Cu on the surface reacts with N_2O by the reaction in Eq. 4 and is converted into Cu_2O.

$$N_2O + 2Cu \leftrightarrow N_2 + Cu_2O \tag{4}$$

After N_2O chemisorption, the sample was cooled to 60 °C, while maintaining a helium balance of 50 ml/min for 1 h. In the 2nd H_2-TPR step, the sample was heated from 60 °C to 300 °C at a rate of 10 °C/min and a flow rate of 50 ml/min of 5% H_2/Ar. Cu_2O (Cu of the surface of sample was converted to Cu (Cu^0) during the 2nd H_2-TPR step. The peak area of the first TPR profile (A_1) corresponds to the amount of CuO in the sample, and that of the second TPR profile (A_2) is the amount of Cu_2O produced by N_2O oxidation. Dispersion of Cu (D*) was calculated as $D^* = 2A_2/A_1$, which is defined as the Cu dispersion [25–28]. Assuming that only the surface of Cu is oxidized by N_2O, D* is considered to be a dispersion of Cu (D*), which is defined as the ratio of exposed surface Cu to total Cu. S_{Cu} is the Cu metal surface area per unit weight of the catalyst and was calculated using *Eq.* 5 [25–27].:

$$S_{Cu}\left(m_2/g_{cat}\right) = D \times Av \times Wt_{Cu}\%/\left(100 \times MW_{Cu} \times N_{Cu}\right) \tag{5}$$

where Av is Avogadro's number (6.02×10^{23}), wt_{Cu} % Cu is the copper content (wt %) of the catalyst, MW_{Cu} is the atomic weight of copper (63.5 g/mol), and N_{Cu} is the number of surface copper atoms in the unit surface area. A reported N_{Cu} value of 1.7×10^{19} m^{-2} [29] was used for the calculation of the S_{Cu}, while N_{Cu} values in the range of 1.35×10^{19}–1.68×10^{19} m^{-2} are available for different copper crystal planes [30].

CO_2 Temperature-Programmed Desorption (CO_2-TPD) was performed using AutoChem II (Micromatics Inc., USA). First, the samples (50 mg) were loaded onto the instrument using a U-type cell, and the catalyst samples were reduced using 10% H_2 (N_2 balance) at 50 ml/min and 270 °C for 2 h. After reduction, the sample was cooled to 120 °C, and He was passed through the samples for 1 h for pretreatment. The samples were cooled to 60 °C and maintained at this temperature for 1 h under a 10% CO_2 atmosphere (He balance) at a flow rate of 50 ml/min for CO_2 adsorption. He was passed through the samples at 60 °C for 1 h for purging. Finally, the sample was heated at a rate of 10 °C/min from 60 °C to 900 °C for CO_2-TPD while He was flowed at 50 ml/min. The outlet gas was then passed through a TCD to detect the desorbed CO_2.

X-ray photoelectron spectroscopy (XPS) analysis was performed) with a microfocus monochromatic X-ray source Al-Kα (1486.6 eV) using a Nexsa XPS system (Thermo Scientific) to investigate surface chemical states and elemental compositions of Cu, and CuO in the calcined and reduced catalysts.

Catalytic Performance Test

Methanol synthesis was performed in a fixed-bed reactor (Inconel, 10 mm inner diameter), and the temperature was controlled using an electrical furnace. The catalyst samples (0.5 g) were crushed and sieved to 425–710 µm and loaded into the reactor tube at a feed gas hourly space velocity (GHSV) of 4,444 h^{-1}. Then, the catalysts were reduced using 10 mol % H_2 (N_2 balance) at 1 bar under 270 °C for 2 h. The temperature was increased to 270 °C at a rate of 5 °C/min and was maintained for 2 h. The catalyst samples were then cooled to 170 °C and flushed with N_2 gas for 1 h. The system was compressed and maintained at a pressure of 40 bar. In the general test for CO_2 feeding in the feed gas, the gas mole ratio for methanol synthesis was H_2: CO: CO_2: N_2 = 61.67:23.33:5:10. After passing through the reactor and back pressure regulator to reduce the pressure, the gas product was analyzed using an online gas chromatography (GC) (Agilent 6890N) equipped with a TCD and FID.

The collected liquid samples, including methanol and other by-products, were analyzed for product distribution using an offline GC. The liquid product in the methanol reaction system was collected using a cold trap maintained at −22 °C and analyzed using an offline GC with an FID. The online GC had two parallel paths: a Porapak-Q (Mesh 80/100, 1/8 inch, 2 m) column connected to the TCD detector and an HP-Innowax (30 m × 0.250 mm × 0.25 µm) column connected to the FID detector (split ratio = 200).

The liquid product was collected using a cold trap at − 22 °C and analyzed using offline GC after the reaction. GC (Agilent 7890 A) with an HP-PONA column (50 m × 0.20 mm × 0.5 µm) and FID detector was used for offline analysis of the liquid products. The split ratio of offline GC was fixed at 350. Helium was used as the GC carrier gas. Equations 6–9 summarize the transformation and selectivity calculation formulae, respectively. X_i is calculated by carbon conversion and carbon selectivity is indicated by S_p. Calculation formula for X_i and S_p is shown in and Eqs. 10 and 11 each.

$$X_i(\%) = \frac{F_i^{\text{in}} - F_i^{\text{out}}}{F_i^{\text{in}}} \times 100; i = \text{CO}, \text{CO}_2 \text{and carbon} = \text{CO} + \text{CO}_2 \quad (6)$$

$$S_{\text{p}}(\%) = \frac{F_p^{\text{out}}}{F_C^{\text{in}} - F_C^{\text{out}}} \times 100; C = \text{CO} + \text{CO}_2 \quad (7)$$

$$X_i(\%) = \text{Conversion of feed component/element of } i \quad (8)$$

$$S_P(\%) = \text{Selectivity of product component of } p \quad (9)$$

$$F_i^{\text{in}} = \text{Inlet molar flow rate of component/element } i \quad (10)$$

$$F_i^{\text{out}} = \text{Outlet molar flow rate of component/element } i \quad (11)$$

Results and Discussion

Table 2 presents the molar ratios of the bulk metal and surface components obtained from XRF and XRS analyses. The bulk component molar ratios of 10ZA and 20ZA support the Zn/Al ratio of 1.0 and 2.1, respectively, which are similar to the ratio of the reagent used. However, for 30ZA, the Zn/Al ratio was 2.2. The molar ratios of Zn and Al for C20Z/10ZA, C10Z/20ZA, and C/30ZA were smaller than those of the reagents used. The metal basis molar ratio of the reagent used and the XRF analysis results were different, which was attributed to the loss resulting from the filtering process after less precipitation during the manufacturing process of the support and catalyst. This is thought to be due to losses from a small filtration process after precipitation during manufacturing of the support and catalyst. The discrepancy between the added Zn/Al and actual XRF measurements is presumed to be due to the fact that the metal of all reagents did not form a precipitate during the aging step (5 h) and was filtered in the form of ions during the filtering procedure.

X-ray diffraction (XRD) diagrams for the catalyst support, calcined catalyst, and reduced catalyst are shown in Fig. 2. The study examined different phases related to Cu, Zn, Al, O, C, and H and found that the primary phases were structured. Although numerous phases were observed in the XRD analysis, $ZnAl_2O_4$, ZnO, CuO, Cu_2O, Cu_4O_3, Cu, and Cu were specifically recognized and assessed using the JADE references. (1) ZnO (zincite, hexagonal; JADE Ref. 98-000-0483) of 31.916° (100), 34.568° (002), 36.401° (101), 47.685° (102), etc. (2) $ZnAl_2O_4$ (gahnite, cubic (F);

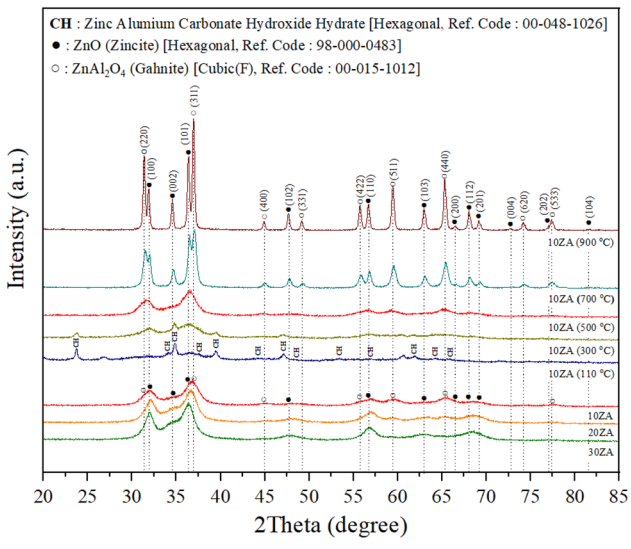

(a) Calcined supports with different calcination temperature (110, 300, 500, 700, and 900 °C and used supports (10ZA, 20ZA, and 30ZA calcined at 500 °C).

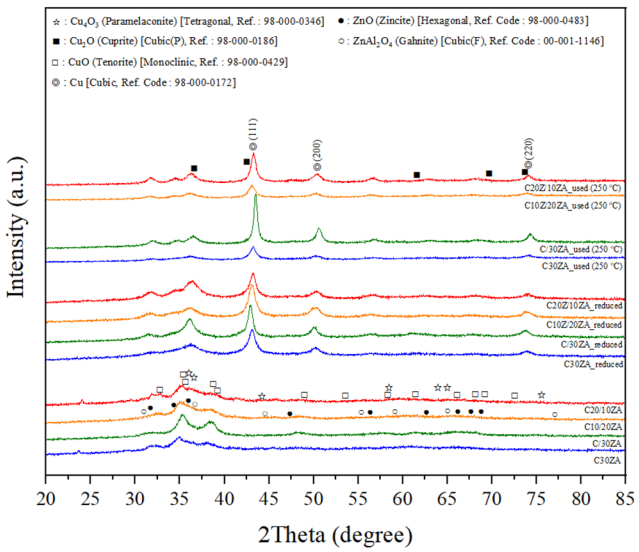

(b) Calcined, reduced catalysts and used catalysts (after reaction at 250 °C, 52 h).

Fig. 2 XRD patterns of support and catalysts

JADE Ref. 00-001-1146) of 31.512° (220), 36.956° (311), 44.983° (400), 55.810° (422), etc. (3) Zinc aluminum carbonate hydroxide hydrate (hexagonal, JADE Ref. 00-048-1026) of 11.838° (033), 23.660° (006), 34.158° (101), 34.871° (012), etc., (4) Cu_4O_3 (tetragonal paramelaconite, JADE Ref. 98-000-0346) of 28.089° (112), 31.030° (103), 35.654° (202), 36.146° (004), 43.834° (220), etc., (5) Cu_2O (cuprite, cubic(P), JADE Ref. 98-000-0186) of 29.392° (110), 36.248° (111), 42.132° (200), 52.285° (211), etc., (6) CuO (tenorite, monoclinic, JADE Ref. 98-000-0429) of 32.531° (110), 35.466° (002), 35.556° (-1,1,1), 38.750° (111), 38.965° (200), etc. (6) Cu (copper, cubic(F), JADE Ref. 98-000-0172) of 43.241° (111), 50.373° (200), and 74.05° (220).

The experiment involved confirming the support and catalyst at each phase location using the JADE program and then indicating the presence of various phases in a complex manner. In Fig. 2, CuO, Cu_4O_3, Cu_2O, ZnO, and $ZnAl_2O_4$ display a peak profile with a wide FWHM when the calcination temperature of the support is 500 °C. Therefore, even when enlarged, they are difficult to visually distinguish. The whole pattern fitting (WPF) method was used to overcome this issue. The existence of these phases was repeatedly assessed, and the results were quantified and presented. The whole pattern fitting (WPF) results according to the Rietveld refinement of the XRD analysis results are shown in Fig. 3.

To determine the presence of ZnO and $ZnAl_2O_4$ phases in the calcined samples, experiments were conducted at various temperatures ranging from 110 °C to 900 °C under air conditions. The samples were dried during calcination, and their XRD analysis results were compared with those of 10ZA, 20ZA, and 30ZA, which were dried during their respective manufacturing processes (Figs. 2a and 3a. 10ZA calcined at 500 °C was the same as the support (10ZA) used in catalyst manufacturing. Some studies have shown that the $Zn_2Al_6O_9$ phase appears calcined at 500 °C, but as a result of the investigation, $Zn_2Al_6O_9$ was not reflected owing to a lack of reference [31].

As shown in Figs. 2a and 3a, when 10ZA was calcined at 110 °C, zinc aluminum carbonate hydroxide hydrate was formed, and it decreased rapidly as the calcination temperature increased; thus, it was not observed at the calcination temperature of 500 °C. ZnO was confirmed in all sections of the calcination temperature in the range of 110–900 °C, which increased rapidly as the calcination temperature increased, and then reached a peak (41%) when the calcination temperature was 500 °C. The ratio of $ZnAl_2O_4$ increased as the calcination temperature increased, reaching 41%, and then increased to 70% when calcined at 900 °C. Figure 2a shows that as the calcination temperature increases by 500 °C or more, the FWHM decreases, and the crystallinity of ZnO and $ZnAl_2O_4$ becomes prominent. However, as the calcination temperature increases, physical properties such as the BET surface area of Support rapidly decrease, so crystallinity itself cannot be linked to catalytic performance [17]. In Figs. 2a and 3a, 10ZA, 20ZA, and 30ZA reveal the absence of zinc aluminum carbonate hydroxide hydrate at a calcination temperature of 500 °C. ZnO was found in all the samples of 10ZA (41%), 20ZA (74%), and 30ZA (96%), but the ratio of $ZnAl_2O_4$-related peaks was higher in 10ZA than in the other catalysts. $ZnAl_2O_4$ was present in 30ZA (4%), but it was weak and ZnO (96%) was the main peak. In

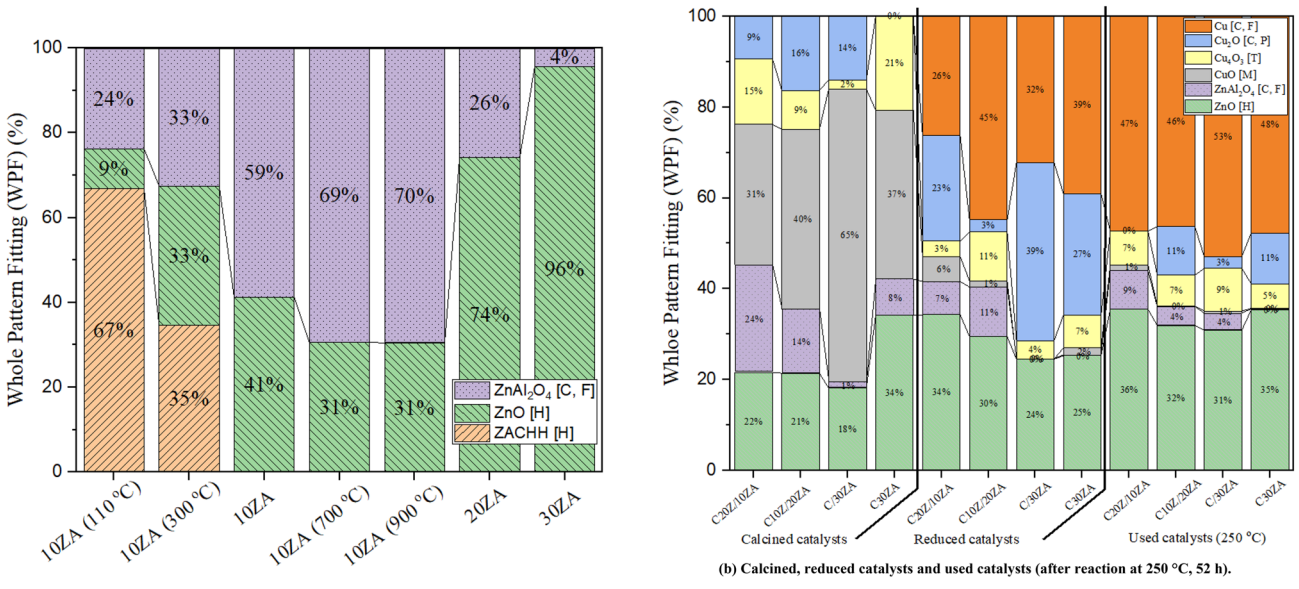

(a) Calcined supports with different calcination temperature and used supports (10ZA, 20ZA, and 30ZA).

(b) Calcined, reduced catalysts and used catalysts (after reaction at 250 °C, 52 h).

Fig. 3 Results of whole pattern fitting (WPF) from XRD patterns of support and catalysts

Table 3 Catalytic characterization of catalysts and reduced catalysts

Sample code	N_2 physi-sorption and desorption results (BET)[a]				Dispersion of copper (%)[b]	Specific surface area of copper ($m^2_{Cu}/g_{Cat.}$)[c,d]	Copper particle size (nm) (N_2O chemisorption)[d]	Cu (111) crystallite size of reduced catalyst (nm) [e]
	BET surface area (S_{BET}) [m^2/g][a]	Monolayer adsorption amount (Vm) [cm^3/g cat.]	Total pore volume [cm^3/g cat.]	Mean pore diameter [nm]				
10ZA	118.3	27.17	0.293	9.90	–	–	–	–
20ZA	94.93	21.81	0.323	13.63				
30ZA	93.21	21.42	0.333	14.30				
C20Z/10ZA [reduced]	70.61 [56.00]	16.22 [12.87]	0.208 [0.184]	11.77 [13.14]	39.4	137.8	3.0	9.7
C10Z/20ZA [reduced]	76.84 [61.24]	17.65 [14.07]	0.347 [0.272]	18.06 [17.73]	44.2	161.7	2.7	9.6
C/30ZA [reduced]	68.67 [47.69]	15.78 [10.96]	0.263 [0.195]	15.34 [16.36]	36.2	124.2	3.3	12.3
C30ZA [reduced]	82.83 [43.00]	5.71 [9.88]	0.107 [0.196]	17.20 [18.25]	47.3	157.5	2.5	9.2

[a]Measured by Moonsorp-I (KIST, Korea)

[b]D* was calculated as $D^* = 2A_2/A_1$, which is defined as the Cu dispersion. [A_1: 1st H_2-TPR area, A_2: 2nd H_2-TPR area]

[c]N_2O titration: 2-step H_2-TPR and N_2O-TPD was measured using AutoChem II, KIST. [Assumed for N_2O titration: 1st TPR area: $CuO + H_2 \rightarrow Cu + H_2O$; 2nd TPR area: $Cu_2O + H_2 \rightarrow 2Cu + H_2O$]

[d]Copper specific surface area, Scu ($m^2/g_{cat.}$) = D x Av x wt_{Cu} % x Mw_{Cu} x N_{Cu}. Av: Avogadro's number (6.02×10^{23}), wt_{Cu}% ($g_{Cu}/g_{cat.}$): Cu content of the catalyst (MW_{Cu}) S_{Cu} (m^2/g_{cat}) = (D x Av x (wt_{Cu}% /100))/(MW_{Cu} x N_{Cu}) MW_{Cu}: The atomic weight of copper (63.5 g/mol) N_{Cu}: The number of surface copper atoms in the unit surface area.: 1.7×10^{19} m^{-2}

[e]Calculated by Debye–Scherrer equation from XRD diffraction data

comparison, high proportions of $ZnAl_2O_4$ were identified in 10ZA (59%) and 20ZA (26%) samples.

In Figs. 2b and 3b, ZnO and $ZnAl_2O_4$ were identified in all calcined catalysts except C/30ZA. In particular, high ratios of $ZnAl_2O_4$ were found in C20Z/10ZA (24%) and C10Z/20ZA (14%), indicating the presence of a phase in the support used was indicated. It was confirmed that Cu_4O_3, CuO, and Cu_2O were present in calcined C20Z/10ZA, C10Z/20ZA, and C30ZA, respectively, but only CuO and Cu_2O were observed in calcined C/30ZA, and Cu_4O_3 was hardly detected. Cu_2O was not observed for the C30ZA catalyst. Cu (cubic (F)) was confirmed from the reduction catalysts shown in Figs. 2b and 3b, and it was confirmed that Cu_2O coexisted. Cu_2O, Cu_4O_3, and CuO in the reduction catalyst were formed by reaction with air when the catalyst was removed from the reactor for analysis. In Fig. 2b, the position of the Cu peak may be finely shifted to the left and may not seem to fit, which is a symptom that occurs when the Cu of the catalyst is oxidized after reduction to generate a small amount of oxide such as Cu_2O. As shown in Table 3, the Cu (111) particle size of the reduction catalyst decreased in the following order: C/30ZA (12.3 nm) > C20Z/10ZA (9.7 nm) > C10Z/20ZA (9.6 nm) > C30ZA (9.2 nm). The order of the Cu particle size estimated by the N_2O concentration analysis results was C/30ZA (3.3 nm) > C20Z/10ZA (3.0 nm) > C10Z/20ZA (2.7 nm) > C30ZA (2.5 nm), which is consistent with the XRD analysis results (Table 3). In the reduction catalyst, $ZnAl_2O_4$ was found in C20Z/10ZA (7%) and C10Z/20ZA (1%) and was rarely observed in C/30ZA and C30ZA (2%). $ZnAl_2O_4$ was identified in C20Z/10ZA (9%), C10Z/20ZA (4%), and C/30ZA (4%) catalysts after 52 h of reaction at 250 °C. It can be estimated that there was a change between ZnO and $ZnAl_2O_4$ during the catalytic reaction. No Zn phase was observed in the supports, calcination catalysts, reduction catalysts, or used catalysts.

Table 3 shows the BET (Brunauer–Emmett–Teller) surface areas of the support, calcination catalyst, and reduction catalyst as well as their changes. While increasing the calcination temperature of the Zn-Al support from 110 °C to 500 °C, the Zn aluminum carbonate hydroxide in the drying stage (110 °C) was converted into ZnO and Zn-Al oxides, resulting in the conversion of intermediate pores into mesopores and the formation of some macropores. In the second coprecipitation step, the BET surface area decreased as Cu and Zn were added to the support, because the concentration of Cu in the catalyst was high, and new pores were formed after Cu was added. 10ZA, which has a relatively high ratio of aluminum, showed a higher BET surface area than those of 20ZA and 30ZA. Among the four calcined catalysts, the BET surface area of C30ZA was the highest at 82.83 m^2/g_{cat}. C/30ZA exhibited the lowest BET surface area of 68.67 m^2/g_{cat}. This is related to C/30ZA, which has a higher CuO content than Cu_4O_3. In the case of C30ZA, Vm and total pore volume after

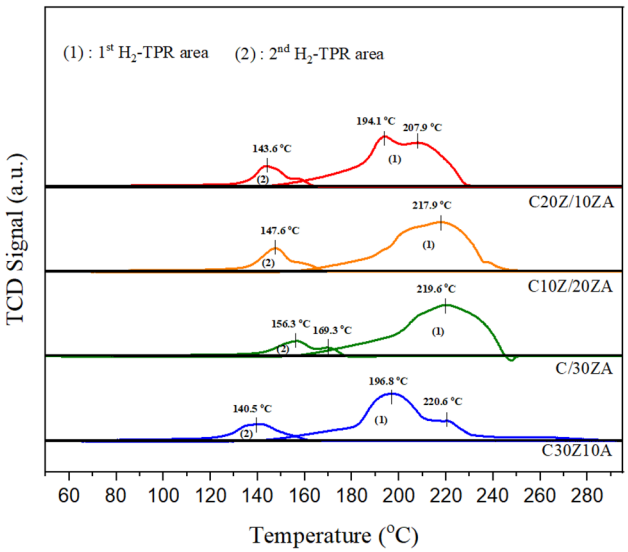

Fig. 4 Two-step H_2-TPR and N_2O-titration profiles of the prepared catalysts

calcination increased after reduction. After the reduction step, the BET surface area of the four catalysts decreased by 20.7–48.1%. C20Z/10ZA, C10Z/20ZA, and C/30ZA manufactured by the two-step coprecipitation method showed higher BET surface areas than C30ZA (43.0 $m^2/g_{cat.}$) after the reduction step, respectively. C30ZA showed the highest BET surface area reduction rate (-48.1%). C20Z/10ZA and C10Z/20ZA exhibited a higher BET surface area than C/30ZA and C30ZA at the time of reduction and also exhibited lower BET surface area reduction rates at the time of reduction. This is related to the higher $ZnAl_2O_4$ phase peaks compared to those of C/30ZA and C30ZA, and it was determined that $ZnAl_2O_4$ affects the sintering and phase change of the catalyst under hydrogen reduction conditions at 270 °C. The melting point of copper is approximately 1085 °C, which is much higher than the reduction temperature (270 °C) of the catalyst; however, sintering of copper nanoparticles may occur at this temperature. $ZnAl_2O_4$ in the catalyst seems to help maintain the structure of the Cu particles, especially when the copper catalyst is reduced by hydrogen, supporting the reduction of copper nanoparticles, thereby maintaining a more stable phase under the same reaction conditions.

The H_2-TPR profiles of the calcined catalysts match the results shown in Fig. 4, with the maximum temperature of the H_2 reduction peak below 290 °C for each catalyst. The Cu–ZnO/mixture of ZnO and Zn-Al Oxide catalyst displayed a higher H_2-TPR peak temperature than that of the C30ZA catalyst. The highest point of decrease, occurring at a temperature above 220 °C, can be attributed to the reduction of the CuO phase and Cu_4O_3), while the shoulder peaks might be due to the stepwise reduction of $Cu^{+2} \rightarrow Cu^{+1} \rightarrow Cu^0$ [8, 32]. The interaction between copper oxide and the support was observed in the order of C20Z/10ZA (219.6 °C), C10Z/20ZA (217.9 °C), C/30ZA (219.6 °C), and C30ZA (220.6 °C) based on the position of the H_2-TPR profile. In the case of the Cu–ZnO/mixture of ZnO and Zn-Al oxide catalyst, it may be seen that the H_2-TPR area at 220 °C or higher is relatively higher than that of C30ZA, and it may be seen that more energy is required for reduction. This seems to have affected the attraction between the support and the copper particles composed of ZnO and $ZnAl_2O_4$ in the case of the Cu–ZnO/mixture of ZnO and Zn-Al oxide catalysts, resulting in an increase in the temperature required for the hydrogen reduction of Cu oxide. The first H_2-TPR area was in the following order: C/30ZA (5.612) > C20Z/10 (5.492) > C10Z/20ZA (5.110) > C30ZA (4.864). In Fig. 3b, the calcined C/30ZA mainly had CuO more than Cu_4O_3 as an oxidation form of Cu. It was found that there was more H_2 required for reduction and higher reduction areas at 220 °C or higher than those of the other catalysts.

N_2O titration analysis was carried out using a two-step H_2-TPR analysis to determine the surface area of the reduced copper and predict the performance of the Cu-based methanol synthesis catalysts, as shown in Table 3 and Fig. 4.

The dispersion of Cu on the reduced catalyst was in the order of C30ZA (47.3%) > C10Z/20ZA (44.2%) > C20Z/10ZA (39.4%) > C/30ZA (36.2%). The C30ZA catalyst demonstrated the highest copper dispersion of 47.3% at the time of reduction, which was higher than that of the Cu–ZnO/mixture of ZnO and Zn-Al oxide catalyst. Specific surface area of copper is C10Z/20ZA (161.7 $m^2_{Cu}/g_{cat.}$) > C30ZA (157.5 $m^2_{Cu}/g_{cat.}$) > C20Z/10ZA (137.8 $m^2_{Cu}/g_{cat.}$) > C/30ZA (124.2 $m^2_{Cu}/g_{cat.}$). The copper particle size from N_2O titration was in the order of C20Z/10ZA

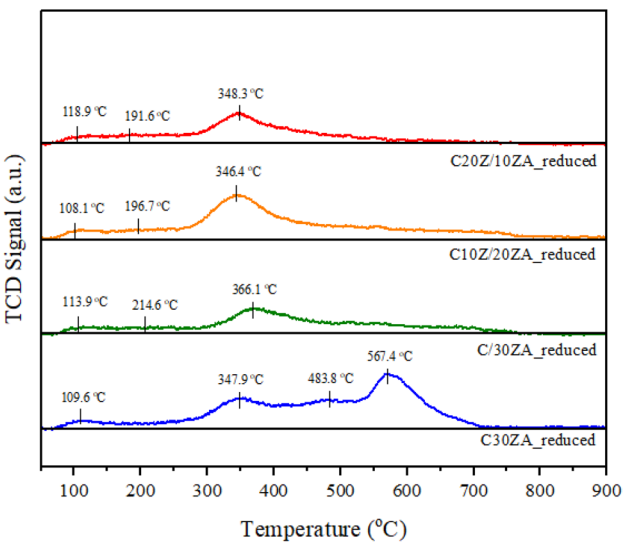

Fig. 5 CO_2-TPD profiles of the reduced catalysts

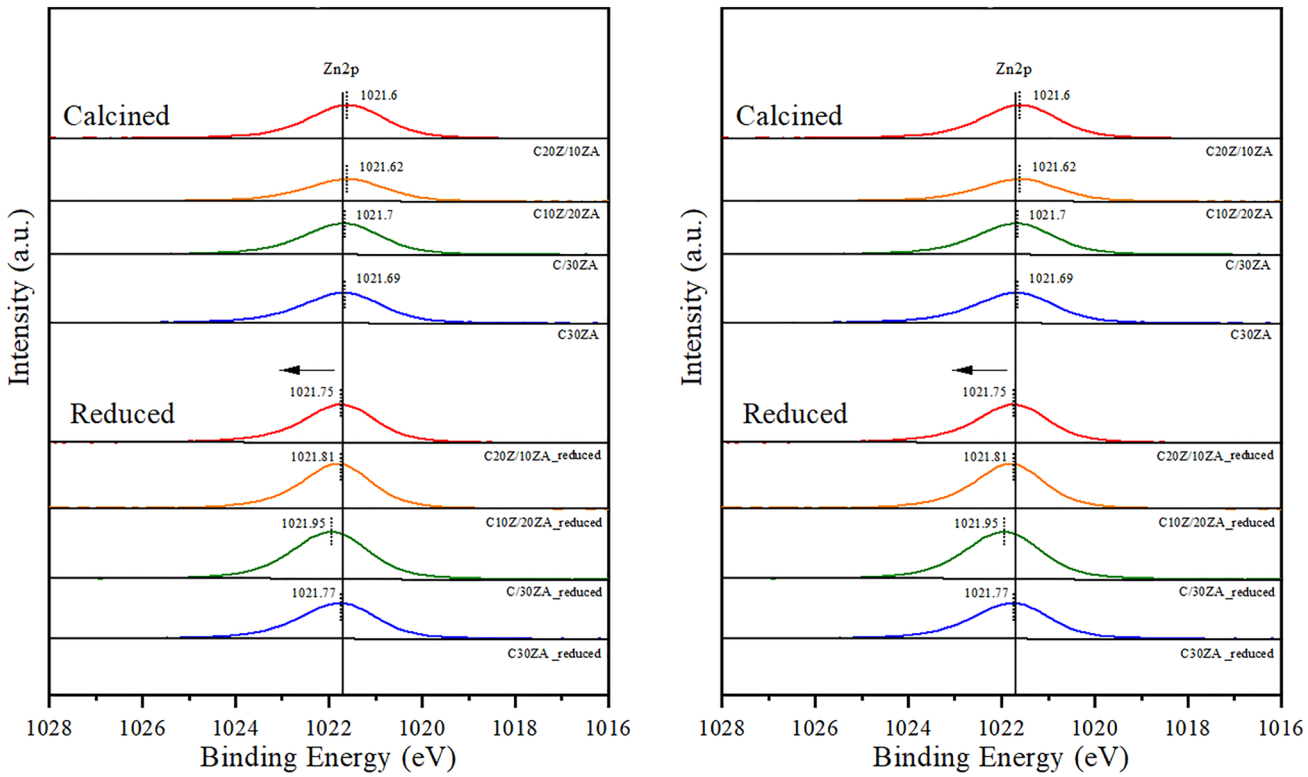

(a) Binding Energy (eV) of Cu2p for calcined and reduced catalysts.

(b) Binding Energy (eV) of Zn2p for calcined and reduced catalysts.

Fig. 6 XPS profiles of the calcined and reduced catalysts

(3.0 nm) > C/30ZA > C10Z/20ZA (2.7 nm) > C30ZA (2.5 nm), which is similar to the trend observed for the Cu (111) particle size from the XRD results. Dispersion of Cu (%) is C30ZA (47.3%) > C10/20ZA (44.2%) > C20Z/10ZA (39.4%) > C/30ZA (36.2%). Owing to the high dispersion and specific surface area of Cu, it can be predicted that C30ZA, C10Z/10ZA will be exhibit higher activity of MeOH production (MeOH yield, $g_{MeOH}/kg_{cat.}/h$) in hydrogenation of Co-feed gas than the other catalysts, owing to the high dispersion of Cu (%) on the reduced catalyst. As shown in Fig. 9, C30ZA afforded a highest MeOH yield (451 $g_{MeOH}/kg_{cat.}/h$) at 250 °C.

The properties of the catalysts were analyzed using the CO_2-TPD and CO_2 desorption profiles, as shown in Fig. 5. The maximum desorption peaks were observed at 300–400 °C for all the catalysts. The TPD profiles were heavily skewed toward higher temperatures, indicating a complex process with multiple CO_2 desorption sites occurring at different underlying sites. The strength of the base sites on the catalysts can be classified as weak, moderate, or strong based on the strength of the base site [33, 34]. Weak sites are associated with surface hydroxyl groups, intermediate base sites are due to metal–oxygen pairs such as Al-O sites, and strong base sites are associated with low coordination oxygen anions [35, 36]. The CO_2-TPD profile was distributed in three regions, corresponding to the desorption of CO_2 in the weak, medium, and strong areas: 150–300 °C, 300–500 °C, and > 500 °C. The catalysts displayed excellent CO_2 desorption properties at approximately 350 °C, and C10Z/20ZA showed the best CO_2 desorption characteristics under these conditions. As shown in Fig. 7, the CO_2 conversion decreased rapidly when the temperature was increased from 250 to 350 °C. C/30ZA had a lower CO_2 desorption area than the other catalysts in the range of 300–400 °C. The C30ZA catalyst shows a remarkable CO_2 desorption peak at 400–700 °C, which may suggest that it has strong base sites and strong CO_2 desorption capacity at temperatures of 400 °C or higher. However, considering that the calcination temperature of C30ZA is 280 °C, this can be seen as a phenomenon caused by gas due to the denaturation of the oxide components for Zn and Al of the catalyst under high-temperature conditions of 400 °C or higher. Further observations are required for certainty.

The high-resolution XPS results for Cu2p in the calcined and reduced catalysts are shown in Fig. 6a. For the calcined catalysts, Cu2p showed wide peaks with a maximum binding energy of approximately 933.45–933.69 eV that could be related to Cu^{2+} in the CuO of the calcined catalysts, also meaning the presence of Cu_4O_3 [37–40]. The peaks of calcined C20Z/10ZA (933.45 eV), C10Z/20ZA (933.61 eV),

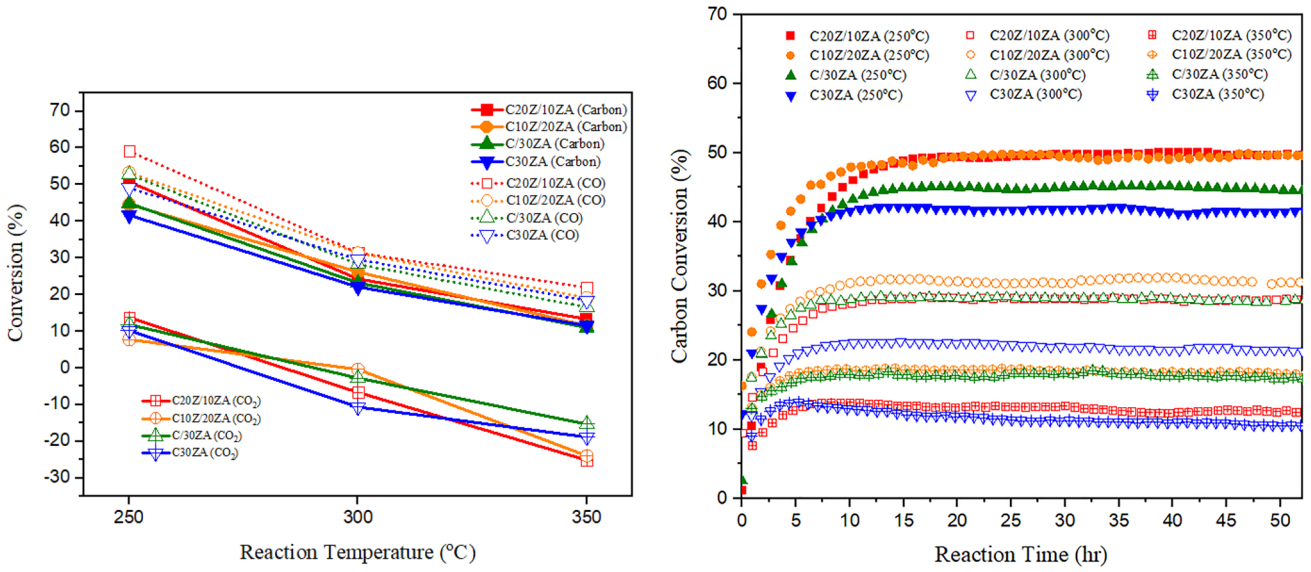

(a) Effect of reaction temperature on the conversion of carbon, CO, and CO_2 [Average of reaction time range: 24-48 h].

(b) Carbon conversion at different temperatures.

Fig. 7 Profiles of carbon ($CO+CO_2$), CO, and CO_2 conversion in the hydrogenation of syngas [Reaction conditions: 0.5 $g_{cat.}$, 40 bar, H_2:CO:CO_2:N_2 = 61.7: 23.3:5:10, GHSV = 4,444 h^{-1}, 250–350 °C, and 52 h]

and C/30ZA (933.52 eV) were in a similar range to those of calcined C30ZA (933.69 eV). Two shakeup satellites near 941–944 eV are also fingerprints of Cu^{2+}. The XRD results showed that calcined C/30ZA had more CuO than Cu_4O_3 (Fig. 1). Calcined C30ZA exhibited a broad and small area under the peaks corresponding to Cu^{2+} compared to the Cu–ZnO/mixture of ZnO and Zn-Al oxide catalysts. For the reduced C30ZA, a peak at 932.5 eV was observed, which can be assigned to Cu^0. This peak has a shoulder at a higher binding energy, which could be related to Cu^{2+}, and shows a small area around 940–944 eV (Fig. 4b). The same trend was observed for the other reduced catalysts, which was similar to that observed for C30ZA. When Cu^{2+} of calcined C30ZA catalysts reduced and Cu^{2+} changed to Cu^0, the peak moved from 933.69 eV to 932.5 eV. Cu^0 peaks of the reduced C20Z/10Z, C10Z/20ZA, and C/30ZA also shifted slightly toward lower binding energies. The Cu^0 peak areas of the reduced catalysts followed the order C10Z/20ZA > C20Z/10ZA > C30ZA ≈ C/30ZA. This shows the trend of Cu^0 on the surface of the catalyst, which differs from the bulk concentration of Cu^0.

When comparing the Cu/Zn molar ratio of the calcined catalyst surface based on the XPS results, it was confirmed that the Cu/Zn ratio to the reduced catalyst was lowered (Table 2). This means that ZnO and $ZnAl_2O_4$ surrounded by Cu oxide in the reduction process are exposed to the surface in the process of reducing Cu oxide, and the Cu/Zn ratio on the surface of the catalyst changes. The surface Cu/Zn molar ratio from the XPS analysis of the calcined catalyst was in the order of C10Z/20ZA (2.7) > C/30ZA (2.3) > C20Z/10ZA (1.9) > C30ZA (1.5). This indicates that the catalyst prepared by the two-step co-precipitation method showed a high Cu/Zn ratio. Compared to the bulk Cu/Zn obtained through XRF analysis, the Cu/Zn molar ratio of XPS before the reduction of C10Z/20ZA (2.2) > C/30ZA (2.1) ≈ C20Z/10ZA (2.1) > C30ZA (1.9) showed a similar tendency to that of the surface Cu/Zn molar ratio of the calcined catalyst by XRF (Table 1). However, the surface Cu/Zn ratio of the reduced catalyst followed the order C10Z/20ZA (1.3) > C20Z/10ZA (1.0) ≈ C30ZA (1.0) > C/30ZA (0.7), which differed from the bulk Cu/Zn ratio results.

In contrast with the Cu phase, the XRD pattern of the reduced catalyst did not show a Zn phase (Fig. 2b). It was confirmed that the binding energy of the Zn2p peak of each catalyst after reduction increased by about 0.08–0.15 eV or more compared to before reduction, and the area of the peak increased (Fig. 6b). ZnO and $ZnAl_2O_4$ all correspond to Zn^{2+} and Zn (Zn^0) is not confirmed, so the change in binding energy is not significant. However, it shows a change in the peak, which is related to the generation of the $ZnAl_2O_4$ phase based on the XRD analysis results. In the case of C/30ZA, $ZnAl_2O_4$ was barely observed at 30ZA before the second coprecipitation, but $ZnAl_2O_4$ was confirmed at C/30ZA after calcination. In addition, $ZnAl_2O_4$ was observed in the catalyst after reduction (Figs. 2 and 3). The presence of small amounts of zinc aluminum carbonate hydroxide hydrate was confirmed in the calcined catalyst, but it was not detected in the catalyst after the reduction and reaction. This is because Zn aluminum carbonate hydroxide undergoes changes in the ZnO or $ZnAl_2O_4$ direction. The

current XPS results alone make it difficult to distinguish between ZnO and $ZnAl_2O_4$, but it can be inferred that the ratio of the two phases increases during the catalyst reduction process.

Figure 7 graphically represents the specific trend of the conversion rates of carbon, CO, and CO_2 during the methanol synthesis reaction for 52 h at 250, 300, and 350 °C. It also shows the average value of each conversion rate for 24–48 h. The amount of catalyst, composition of the raw material, reaction pressure, GHSV, and reaction time were constant, while the reaction temperature was varied. A decrease in the conversion rates of carbon and CO was observed for all four catalysts as the reaction temperature increased from 250 to 350 °C. The CO and CO_2 conversion rates also decreased as the reaction temperature increased. A negative CO_2 conversion rate indicates that the CO_2 in the outlet is greater than the amount of CO_2 in the feed added at 350 °C. The temperature and CO_2 desorption area of CO_2-TPD of each reduced catalyst were high at 350 °C, which confirmed that the conversion rate of CO_2 was low under these conditions (Fig. 5).

When the reaction temperature increases above 300 °C, methanol synthesis and reverse water gas transfer (RWGS) reactions occur simultaneously during the hydrogenation of CO_2. CO can be generated by the RWGS reaction, indicating a decrease in the CO conversion rate. At this time, when the temperature increased, methanol synthesis, an exothermic reaction, was suppressed, but the reverse water gas transfer (RWGS) reaction, which is an endothermic reaction, was strengthened, resulting in a low methanol yield at temperatures above 300 °C [41, 42]. Additionally, it was established that as the reaction temperature increased from 250 °C to 300 °C and then to 350 °C, the methanol selectivity diminished, whereas the selectivity for CH_4 (methanation) and other compounds (higher alcohol synthesis) increased. As the reaction temperature increased, a side reaction of the endothermic reaction occurred (more than 300 °C), and the thermal balance was broken, resulting in the suppression of the formation of reactants, decomposition of reactants, and reverse generation of feed, resulting in a decrease in the equilibrium conversion rate of CO, CO_2, and H_2 (Figs. 7, 8, 9).

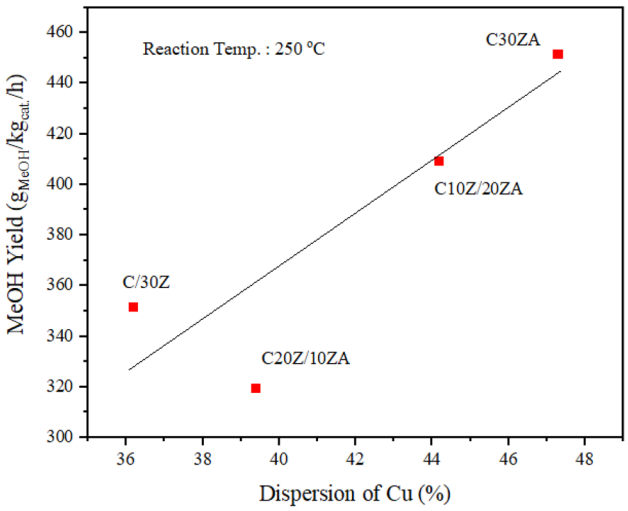

Fig. 9 Relationship between dispersion of Cu (%) with MeOH yield (g_{MeOH}/$kg_{cat.}$/h) over catalysts in the hydrogenation of syngas [Reaction conditions: 0.5 $g_{cat.}$, 40 bar, H_2:CO:CO_2:N_2 = 61.7: 23.3:5:10, GHSV = 4,444 h^{-1}, 250 °C, and 52 h]

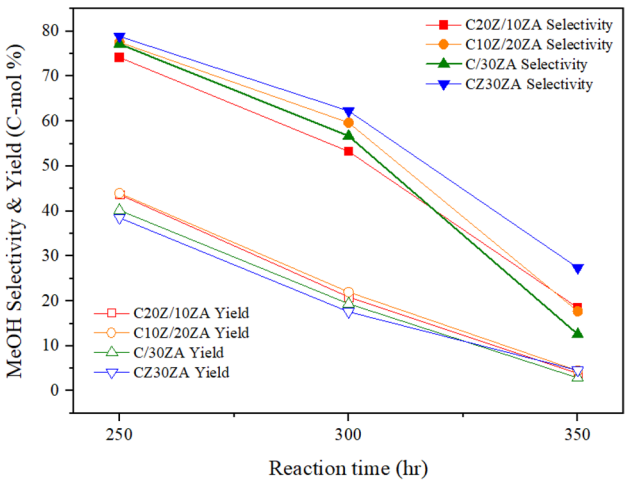

Fig. 8 MeOH selectivity and yield over catalysts in the hydrogenation of syngas [Reaction conditions: 0.5 $g_{cat.}$, 40 bar, H_2:CO:CO_2:N_2 = 61.7: 23.3:5:10, GHSV = 4,444 h^{-1}, 250–350 °C, and 52 h]

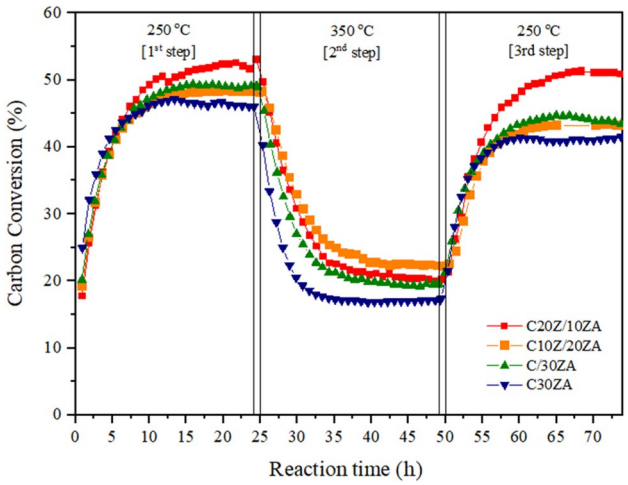

Fig. 10 Profiles of carbon conversion in the order of 1st step (250 °C, 24 h), 2nd step (350 °C, 24 h), and 3rd step (250 °C, 24 h) in the hydrogenation of syngas [Reaction condition: 0.5 $g_{cat.}$, 40 bar, H_2/Carbon ($CO + CO_2$) = 2, and GHSV = 4,444 h^{-1}]

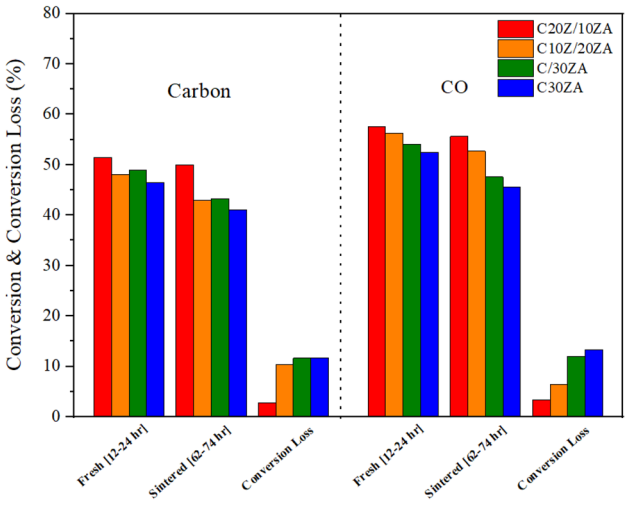

Fig. 11 Summary of carbon, CO, and H_2 conversion loss (%) compared 12–24 h (1st step) with 62–74 h (3rd step) over catalysts in the hydrogenation of syngas after reaction at 250 °C (1st step, 24 h), 350 °C (2nd step, 24 h), and 250 °C (3rd step, 24 h). [Reaction condition: 0.5 $g_{cat.}$, 40 bar, H_2/Carbon $(CO+CO_2)=2$, and GHSV = 4,444 h^{-1}.]

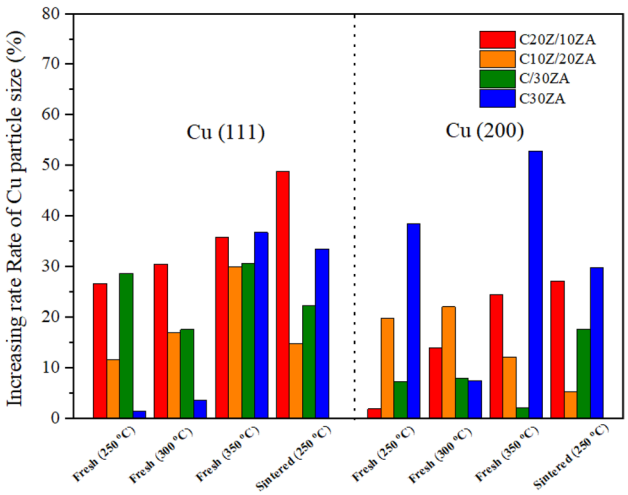

Fig. 12 Increasing rate of Cu particle size at different reaction temperatures with reduced catalyst fresh and sintered catalysts which after the reaction

As shown in Figs. 11 and 12, as the reaction temperature increased to 300 °C and 350 °C, there was a change in the particle size of Cu, but the change in the conversion rate was not significant. The temperature was initially set at 250 °C for 24 h, followed by 24 h of reaction at 350 °C, and then returned to 250 °C for another 24 h, resulting in reactivity that allowed it to regain its initial conversion rate at 250 °C (Fig. 10). Therefore, the reduction in the conversion rates of carbon, CO, CO_2, and H_2 could not be explained by the sintering of Cu.

Figure 8 summarizes the results of the product obtained after MeOH synthesis according to carbon selectivity. At this time, the products were divided into gas and liquid products, and the liquid products were based on products collected in cold traps at − 22 °C and 40 bar to obtain the MeOH yield. The methanol selectivity of the catalysts was higher than 70% at 250 °C and 40 bar for the feed using a $CO/CO_2/H_2$ mixture as the raw material. Under the reaction conditions of 250 °C, a methanol selectivity of 74 C-mol% or more could be confirmed in all catalysts under reaction conditions of 250 °C. C20Z/10ZA (74.2 C-mol %), C10Z/20ZA (77.6 C-mol %), C/30ZA (77.2 C-mol %), C30ZA (78.9 C-mol %). The dispersibility (%) of Cu in each reduction catalyst was obtained through N_2O titration and is C30ZA (47.3%) > C10/20ZA (44.2%) > C20Z/10ZA (39.4%) > C/30ZA (36.2%). Methanol yield at the reaction conditions of 250 °C for 52 h is C30ZA (451.3 $g_{MeOH}/kg_{cat.}/h$) > C10Z/20ZA (409 $g_{MeOH}/kg_{cat.}/h$) > C/30ZA (351.3 $g_{MeOH}/kg_{cat.}/h$), followed by C20Z/10ZA (319.4 $g_{MeOH}/kg_{cat.}/h$), which was similar to the dispersion of Cu (%) in the reduced catalyst. This trend was established only at 250 °C, where methanol production was the main reaction. When the reaction temperature rises above 300 °C, CO_2 or methane is generated by the Reverse water gas shift and methanation reactions, and although not reflected in the results of this experiment, side reactions such as dimethyl ether (DME) could be generated [43].

CO_2 hydrogenation to methanol is equilibrium-limited by high temperature. Generally, a catalyst efficiently operates at high temperatures, which requires exceptional thermal stability.

The conversion of carbon dioxide into methanol is hindered by equilibrium at high temperatures.

The analysis revealed small amounts of C_{6-13} olefins and paraffin in the liquid products, which were considered as part of other factors when calculating the selectivity. The analysis confirmed the presence of gaseous products such as methane, DME, C_{2-4} olefin, and paraffin, except for MeOH, and the presence of liquid products such as C_{5-13} paraffin, C_{4-13} olefin, ethanol, propanol, and butanol were confirmed. Higher alcohols were produced during the reaction experiments, with methanol, ethanol, n-C_3 alcohol, and n-C_4 alcohol being produced in the following amounts: methanol > ethanol > n-C3 alcohol > n-C_4 alcohol. The carbon mol% of MeOH in the liquid methanol product recovered from the cold trap after the reaction was 93% or more. Therefore, when developing a methanol manufacturing process using this catalyst, a distillation process must be implemented to obtain high-purity methanol.

The Cu–ZnO/mixture of ZnO and Zn-Al oxide catalyst was found to have a higher resistance to sintering in high-temperature reactions than C30ZA, which exhibited good thermal stability, as evidenced by the changes in carbon

conversion (Figs. 10 and 11). The conversion losses of the catalysts used for carbon and CO are shown in Fig. 11. For reaction temperatures of 250, 300, and 350 °C for 52 h, they were labeled 'Fresh.' The resulting measurement, labeled "Sintered," was obtained by conducting a 24 h reaction at 250 °C (1st step), followed by a 24 h reaction at 350 °C (2nd step) and another 24 h reaction at 250 °C (3rd step). The conversion loss of 'Sintered' was calculated as the change between the carbon and CO conversion rates in the 12–24 h segment (1st step) at 250 °C and 62–74 h segment (3rd step) at 250 °C. Figure 11 reveals that the C30ZA catalyst had higher carbon (11.7%) and CO (13.3%) losses than those of the C20Z/10ZA, C10Z/20ZA, and C30ZA catalysts. Among these, the C20Z/10ZA catalyst showed the lowest carbon conversion loss (2.8%), CO conversion loss (3.3%), and highest thermal stability.

Figure 12 summarizes the particle size change rate for Cu (111) and Cu (200) of the catalyst after the reaction, based on the size of the Cu particles of the catalyst when reduced at 250, 300, and 350 °C for 52 h each. In addition, the Cu particle size of the reacted catalyst by changing the temperature in the order of 250 °C (1st step, 24 h), 350 °C (2nd step 24 h), and 250 °C (3rd step, 24 h) was also calculated and expressed as 'Sintered.' At this time, the smaller the size change of the reduced catalyst compared to the Cu particles, the less sintering of Cu occurred. It can be observed that the C10Z/20ZA, C20Z/10ZA, and C/30ZA catalysts, which involve co-precipitation of Cu and Zn in a mixture of ZnO and Zn-Al oxide, have higher thermal durability against Cu sintering compared to C30ZA. Specifically, after reacting for 52 h at 250 °C, C30ZA exhibited the highest level of Cu sintering (38.5%), followed by C20Z/10ZA (19.8%), C/30ZA (7.2%), and C10Z/20ZA (1.9%). Similarly, after reacting for 52 h at 350 °C, C30ZA exhibited the highest level of Cu sintering (52.9%), followed by C20Z/10ZA (24.5%), C10ZA (12.1%), and C/30ZA (2.1%). Moreover, the results showed that C30ZA (29.8%), C20Z/10ZA (27.2%), C/30ZA (17.7%), and C10Z/20ZA (5.3%) exhibited the highest level of Cu sintering. Through the change in carbon conversion rate, the size of the Cu (200) particles, and the XRD results, it was confirmed that the Cu–ZnO/(a mixture of ZnO and Zn-Al oxide) catalyst suppressed the sintering of Cu by the synergy of the mixture of ZnO and $ZnAl_2O_4$ and reduced Cu, and thus had better thermal stability than the C30ZA catalyst. Therefore, in terms of the long-term stability of the MeOH production reaction, Cu–ZnO/mixture of ZnO and Zn-Al oxide catalyst is considered to be superior in overall yield compared to the C30ZA catalyst, and more optimized research is needed. Therefore, it was confirmed that the two-step co-precipitation method for preparing a Cu–ZnO/mixture of ZnO and $ZnAl_2O_4$ was superior to the catalyst prepared by the one-step co-precipitation method, which can be assumed to be excellent for long-term reactions at 250 °C, which is the methanol manufacturing temperature. As a follow-up study, we will conduct an optimization study on the manufacturing method of the Cu-based catalyst using the support and support of this catalyst, and if we find a way to improve the Cu specific surface area of the reduced catalyst, we will develop a catalyst with long-term stability and high methanol yield.

Conclusions

A modified Cu–ZnO/mixture of ZnO and Zn-Al oxide catalyst was prepared using a two-step co-precipitation method (C30Z/10ZA, C10Z/20ZA, and C/30ZA) and compared with a catalyst prepared using the one-step co-precipitation method (C30ZA). XRD analysis with WPF confirmed that all the catalysts (C20Z/10ZA, C10ZA, and C/30ZA) contained ZnO and $ZnAl_2O_4$. In the case of C20Z/10ZA and C20Z/10ZA, the ratio of $ZnAl_2O_4$ was higher than C/30ZA and C30ZA. The specific surface area of Cu on the catalysts obtained by N_2O titration was in the order C10Z/20ZA > C30ZA > C20Z/10ZA > C/30ZA, and it was confirmed that the particle size of C30ZA with a lower dispersion of copper was the smallest. The XRD results showed that the Cu particle size of the reduced catalyst followed the same trend as that of the N_2O titration. As a result of hydrogenation of a mixed gas of CO and CO_2 as raw materials, the conversion rates of carbon, CO, and CO_2 decreased as the reaction temperature increased. Methanol yield at the reaction conditions of 250 °C for 52 h is C30ZA (451.3 $g_{MeOH}/kg_{cat.}/h$) > C10Z/20ZA (409 $g_{MeOH}/kg_{cat.}/h$) > C/30ZA (351.3 $g_{MeOH}/kg_{cat.}/h$), followed by C10Z/20ZA (319.4 $g_{MeOH}/kg_{cat.}/h$), which was similar to the dispersion of Cu (%) in the reduced catalyst. In the methanol synthesis reaction under fresh or sintered conditions, it was confirmed that the C10Z/20ZA, C20Z/10ZA, and C/30ZA catalysts showed lower loss of Carbon and CO conversion rates than the C30ZA catalysts, and the rate of increase in the Cu particle size after the reaction was also low. Also, it can be found that the C10Z/20ZA and C20Z/10ZA catalysts with higher Zn-Al oxide ratios have higher thermal durability against Cu sintering than C30ZA and C/30ZA.

In addition, compared to the C30ZA catalyst manufactured by the two-step co-precipitation method, the C20Z/10ZA and C10Z/20ZA catalysts improved thermal long-term stability by suppressing the sintering of reduced Cu by attraction between Cu and the mixture of ZnO and Zn-Al oxide manufactured in the first co-precipitation method, which can suggest the development direction of Cu–Zn-Al-based catalysts for MeOH synthesis with increased yield due to improved long-term stability of the catalyst.

Acknowledgements The authors gratefully acknowledge their co-workers for their valuable research.

Declarations

Conflict of interest The authors declare no conflict of interest. This study was supported and funded by the Korea Institute of Science and Technology (Project No. 2E32562). The data presented in this study are available on request from the corresponding authors.

References

1. G. Bozzano, F. Manenti, Prog. Energy Combust. Sci. **56**, 71 (2016)
2. A.R. Richard, M. Fan, Fuel **222**, 513 (2018)
3. M. Behrens, Angew. Chem. Int. Ed. **55**, 14906 (2016)
4. S.A. Kondrat, P.J. Smith, L. Lu, J.K. Bartley, S.H. Taylor, M.S. Spencer, G.J. Kelly, C.W. Park, C.J. Kiely, G.J. Hutchings, Catal. Today **317**, 12 (2018)
5. Y.M. Liu, J.T. Liu, S.Z. Liu, J. Li, Z.H. Gao, Z.J. Zuo, W. Huang, J. CO2 Util. **20**, 59 (2017)
6. M. Bowker, ChemCatChem **11**, 4238 (2019)
7. L. Wang, L. Yang, Y. Zhang, W. Ding, S. Chen, W. Fang, Y. Yang, Fuel Process Techonol. **91**, 723 (2010)
8. H. Jung, D.-R. Yang, O.-S. Joo, K.-D. Jung, Bull. Korean Chem. Soc. **31**, 1241 (2010)
9. X.-M. Liu, G. Lu, Z.-F. Yan, J. Beltramini, Ind. Eng. Chem. Res. **42**, 6518 (2003)
10. J. Nakamura, T. Uchijima, Y. Kanai, T. Fujitani, Catal. Today **28**, 223 (1996)
11. T. Fujitani, J. Nakamura, Catal. Lett. **56**, 119 (1998)
12. J. Bart, R. Sneeden, Catal. Today **2**, 1 (1987)
13. D. Sheldon, Johns. Matthey Technol. Rev. **61**, 172 (2017)
14. S. Ren, W.R. Shoemaker, X. Wang, Z. Shang, N. Klinghoffer, S. Li, M. Yu, X. He, T.A. White, X. Liang, Fuel **239**, 1125 (2019)
15. M.N. Barroso, M.F. Gomez, J.A. Gamboa, L.A. Arrúa, M.C. Abello, J. Phys. Chem. Solids **67**, 1583 (2006)
16. X. Zhang, G. Zhang, W. Liu, F. Yuan, J. Wang, J. Zhu, X. Jiang, A. Zhang, F. Ding, C. Song, Appl. Catal. B **284**, 119700 (2021)
17. H.-T. Song, A. Fazeli, H.D. Kim, A.A. Eslami, Y.S. Noh, N.G. Saeidabad, D.J. Moon, Fuel **283**, 118987 (2021)
18. P. Mierczynski, T.P. Maniecki, K. Chalupka, W. Maniukiewicz, W.K. Jozwiak, Catal. Today **176**, 21 (2011)
19. L. Song, H. Wang, S. Wang, Z. Qu, Appl. Catal. B Environ. **322**, 122137 (2023)
20. S. Wang, L. Song, Z. Qu, Chem. Eng. J. **8**, 144008 (2023)
21. S. Radha, J. Mani, R. Rajkumar, M. Arivanandhan, R. Jayavel, G. Anbalagan, Mater. Res. Express **10**, 025501 (2023)
22. A. Kiennemann, H. Idriss, J. Hindermann, J. Lavalley, A. Vallet, P. Chaumette, P. Courty, Appl. Catal. **59**, 165 (1990)
23. W.S. Kim, D.R. Yang, D.J. Moon, B.S. Ahn, Chem. Eng. Res. Des. **92**, 931 (2014)
24. H. Jung, D.R. Yang, K.D. Jung, Bull. Korean Chem. Soc. **36**, 2875 (2015)
25. A. Fazeli, A.A. Khodadadi, Y. Mortazavi, H. Manafi, Iran. J. Chem. Chem. Eng. **32**, 45 (2013)
26. S. Sato, R. Takahashi, T. Sodesawa, K.-I. Yuma, Y. Obata, J. Catal. **196**, 195 (2000)
27. J.R. Jensen, T. Johannessen, H. Livbjerg, Appl. Catal. A: Gen. **266**, 117 (2004)
28. Z. Chen, X. Zhao, S. Wei, D. Wang, X. Zhang, J. Shan, Korean J. Chem. Eng. **39**, 2983 (2022)
29. B. Sundquist, Acta Metall. **12**, 67 (1964)
30. E. Giamello, B. Fubini, P. Lauro, A. Bossi, J. Catal. **87**, 443 (1984)
31. T. Wang, X. Wang, Y. Gao, Y. Su, Z. Miao, C. Wang, L. Lu, L. Chou, X. Gao, J. Energy Chem. **24**, 503 (2015)
32. K. Sonobe, M. Tanabe, T. Imaoka, W.J. Chun, K. Yamamoto, Chem. Eur. J. **27**, 8452 (2021)
33. C. Zhong, X. Guo, D. Mao, S. Wang, G. Wu, G. Lu, RSC Adv. **5**, 52958 (2015)
34. C.R. Second, E. Edition, G. Ertl, H. Knözinger, F. Schüth, J. Weitkamp, W.V.V.G. KGaA, Co, Handbook of heterogeneous catalysis, 2008.
35. P. Gao, F. Li, F. Xiao, N. Zhao, W. Wei, L. Zhong, Y. Sun, Catal. Today **194**, 9 (2012)
36. Y. Zhang, L. Zhong, H. Wang, P. Gao, X. Li, S. Xiao, G. Ding, W. Wei, Y. Sun, J. CO2 Util. **15**, 72 (2016)
37. V.D. Dasireddy, N.S. Štefančič, M. Huš, B. Likozar, Fuel **233**, 103 (2018)
38. N. Chotigkrai, P. Tannititam, S. Piticharoenphun, N. Triamnak, S. Praserthdam, P. Praserthdam, Korean J. Chem. Eng. **39**, 920 (2022)
39. Y. Alajlani, F. Placido, A. Barlow, H.O. Chu, S. Song, S.U. Rahman, R. De Bold, D. Gibson, Vacuum **144**, 217 (2017)
40. H. Tan, M.N. Hedhill, Y. Wang, J. Zhang, K. Li, S. Sioud, Z.A. Al-Talla, M.H. Amad, T. Zhan, O.E. Tall, Catal. Sci. Technol. **3**, 3360 (2013)
41. X. Fang, Y. Men, F. Wu, Q. Zhao, R. Singh, P. Xiao, L. Liu, T. Du, P.A. Webley, Korean J. Chem. Eng. **38**, 747 (2021)
42. L. Grabow, M. Mavrikakis, ACS Catal. **1**, 365 (2011)
43. Z. Azizi, M. Rezaeimanesh, T. Tohidian, M.R. Rahimpour, Chem. Eng. Process. **82**, 150 (2014)